

Linking microscopic structure to optical properties in soft plasmonic complexes

Francesco Brasili^{1,2,*}, Angela Capocéfalo^{3,*}, Giovanni Del Monte^{1,4}, Rodrigo Rivas-Barbosa², Javier Pérez⁵, Edouard Chauveau⁶, Federico Bordi², Domenico Truzzolillo⁶, Emanuela Zaccarelli^{1,2,†} and Simona Sennato^{1,2‡}

¹*Institute for Complex Systems, National Research Council, Piazzale Aldo Moro 5, 00185, Rome, Italy*

²*Department of Physics, Sapienza University of Rome, Piazzale Aldo Moro 5, 00185, Rome, Italy*

³*Department of Physical and Chemical Sciences,*

University of L'Aquila, Via Vetoio, Coppito, 67100, L'Aquila, Italy

⁴*Soft Condensed Matter and Biophysics, Debye Institute for Nanomaterials Science,*

Utrecht University, Princetonplein 1, 3584 CC, Utrecht, The Netherlands

⁵*Synchrotron SOLEIL, L'Orme des Merisiers, Départementale 128, 91190 Saint-Aubin, France*

⁶*Laboratoire Charles Coulomb, UMR 5221, CNRS–Université de Montpellier, 34095, Montpellier, France and*

Abstract

The complexation of plasmonic nanoparticles (NPs) and thermoresponsive microgels is widely exploited for applications. Yet, a microscopic description of the mechanisms governing spatial organization of the NPs is still lacking. Combining small angle X-ray scattering, state-of-the-art numerical simulations and a simple toy model, we uncover how the volume phase transition of microgels drives NP-NP interactions, inducing NP progressive rearrangement with temperature. These results are directly compared to the extinction spectra of microgel–NPs complexes, allowing us to establish for the first time a microscopic link between plasmon coupling and NP local structure.

* These authors contributed equally to this work

† emanuela.zaccarelli@cnr.it

‡ simona.sennato@cnr.it

Soft polymeric colloids such as microgels have prompted significant advancements in soft matter physics as well as nanotechnology, owing to their peculiar properties arising from the combination of colloidal and polymeric nature [1–4]. In particular, the possibility of tuning softness and temperature responsiveness by modifying the chemical composition of the polymer network is not only ideal to investigate fundamental problems in condensed matter physics [3, 5, 6], but also offers the opportunity to design novel photonic materials through integration with plasmonic nanoparticles (NPs) [7–11]. This exploits the volume phase transition (VPT) of thermoresponsive microgels, *i.e.* their reversible collapse in response to temperature increase, for tailoring the collective optical properties of NPs [12, 13]. In fact, the fine-tuning of the resonant absorption and scattering of light by NPs, taking place at the localized surface plasmon resonance (LSPR), can be achieved through the coupling between nearby NPs, which occurs for surface-to-surface distances of few nanometers and depends on NPs spatial organization [14]. Despite great practical relevance, little attention has been given to obtain a fundamental understanding of the microscopic details of NPs incorporation within the soft colloids. This involves the knowledge of the correlations among particles confined to a spherical surface, an important physical problem often studied theoretically [15–18] and sometimes experimentally [19, 20], but never applied to study microgel–NPs complexes.

In this Letter, we fill this gap by combining Small Angle X-ray Scattering (SAXS) experiments and molecular dynamics simulations to study the temperature-dependent arrangement of gold NPs adsorbed onto thermoresponsive microgels by means of electrostatic interactions. For the first time, we are able to connect the spatial organization of the NPs on the microgel with the optical properties of the complexes. We find that upon increasing temperature, NPs get closer due to microgel shrinking, but they do not form clusters. Rather, they try to maximize their distance in order to reduce their mutual electrostatic repulsion. To unveil this behavior, we employ a simple model of NPs arranged on a spherical shell, which qualitatively describes the complex experimental and numerical NP structure factors embedded within the spherical surface of the microgel. Thanks to this approach, we are able to establish the relationship between the degree of plasmon coupling and NP–NP distance, independent on the number of employed NPs, offering a pivotal step towards a strict control of the optical response of soft plasmonic complexes.

We employ cationic poly(N-isopropylacrylamide) (pNIPAM) microgels interacting with

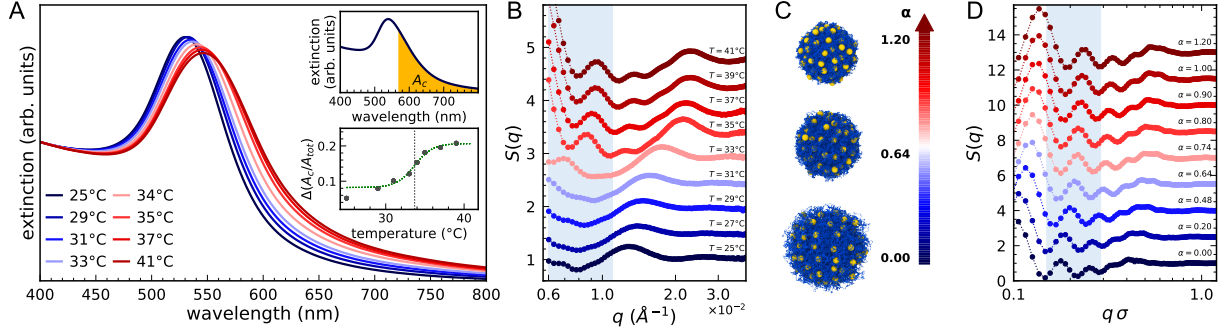


FIG. 1. (A) Optical properties of the microgel–NPs complexes: extinction spectra for different temperatures for the sample with $n = 150$; top inset, region of coupled plasmon modes (orange, A_C) used to define the degree of coupling $\Delta(A_C/A_{tot})$ (Eq. S1, details in SM); bottom inset, $\Delta(A_C/A_{tot})$ as a function of T and sigmoidal fit (dashed line) yielding a critical temperature $T_C = 33.7 \pm 0.2^\circ\text{C}$. (B) Experimental structure factors of NPs adsorbed onto microgels at different temperatures. (C) Snapshots of the simulated system for three representative values of the effective temperature α ; blue and yellow particles represent microgel monomers and NPs, respectively. (D) Numerical structure factors of NPs adsorbed onto a microgel with $N = 112k$ and $f = 0.02$ for $n = 150$ at different values of α . Curves in panels (B) and (D) are vertically shifted for clarity; the light blue color highlights the peak mostly described in the text.

anionic gold NPs and analyze the samples by extinction spectroscopy and SAXS at varying temperatures to establish a relation between optical properties and structural modification across the VPT (see experimental methods in Supplemental Material, SM). We focus on NP/microgel number ratios $n = 150$ (Fig. 1) and $n = 300$ (Fig. S1), since these conditions yield a high NPs coverage as detailed in the SM. Extinction spectra, reported in Fig. 1A, show that the LSPR evolves with increasing temperature, exhibiting a redshift and a slight quenching as well as an increase in the extinction at larger wavelengths. These spectral changes are the signature of plasmon coupling, that is the activation of low-energy collective modes, arising from plasmon hybridization [21] occurring when, driven by the microgel deswelling, NPs approach each other reaching surface-to-surface distances d of a few nanometers (see SM for details). Although most applications involving metallic NPs rely on exploiting plasmon coupling to tune the spectral region in which these systems are optically active, only very recently a first connection between the optical properties of microgel–NPs complexes and the structure of the polymer network was established by the analysis of the

LSPR shift [22]. However, more than the shift, the main feature of interest for colorimetric detection or surface-enhanced spectroscopies is the onset of low-energy modes [23–26]. We thus choose the range between 570 and 800 nm (Fig. 1A) and quantify the degree of coupling from its spectral weight $\Delta(A_C/A_{tot})$ [27, 28], defined in Eq. S1. Notably, by plotting it as a function of temperature in the inset of Fig. 1A, we obtain a sigmoidal-like trend, with an inflection point in correspondence of T_C , demonstrating the possibility to detect the VPT of the microgels through the coupling of the adsorbed NPs.

To go one step further in the microscopic description of NP–NP organization, we measure NP–NP structure factors $S(q)$ as a function of temperature, which are reported in Fig. 1B for $n = 150$. Since the measured SAXS intensities solely arise from NPs, thanks to the much higher contrast of gold with respect to the polymer [7], $S(q)$ ’s are directly obtained by dividing each scattering curve by the form factor of NPs (Fig. S2). Due to the complex structure of the soft assemblies, the interpretation of the curves and their temperature-dependent evolution is far from trivial within the analyzed q -range. In particular, the onset of a new peak at $\sim 1 \times 10^{-2} \text{Å}^{-1}$ (highlighted in light blue) when temperature exceeds $T_C = 33.3 \pm 0.3 \text{ °C}$ (swelling curve in Fig. S3) and the concurrent shift of the large band from $1.2 \times 10^{-2} \text{Å}^{-1}$ to $2.2 \times 10^{-2} \text{Å}^{-1}$ point to a nanoscale rearrangement of NPs across the VPT of the microgels.

These features require detailed microscopic investigation since they outline an interesting route for tuning LSPR exploiting the VPT of the microgels. To this aim, we resort to numerical simulations using a well-established computational model [29], that provides a realistic and accurate description of the polymeric network across the VPT [30], also in presence of charged monomers [31] and upon interactions with charged NPs [32] (see SM for details). In the simulations, the increase of temperature is reproduced by the use of a solvophobic potential between the monomers (Eq. S4), which implicitly accounts for monomer–solvent interaction through a parameter α that plays the role of an effective temperature [33]. Good solvent conditions correspond to $\alpha = 0$, while the affinity to the solvent gets worse as α increases. Simulations are conducted for various α values for single microgels, made of either $N = 14k$ or $N = 112k$ monomers of diameter σ to assess size effects, with a varying fraction f of charged monomers located on the external shell, to mimic the role of the initiators [31], in the presence of varying amounts of NPs and relative counterions, as detailed in the SM. The microgel swelling curve (Fig. S4) displays the shrinking of the microgel–NPs

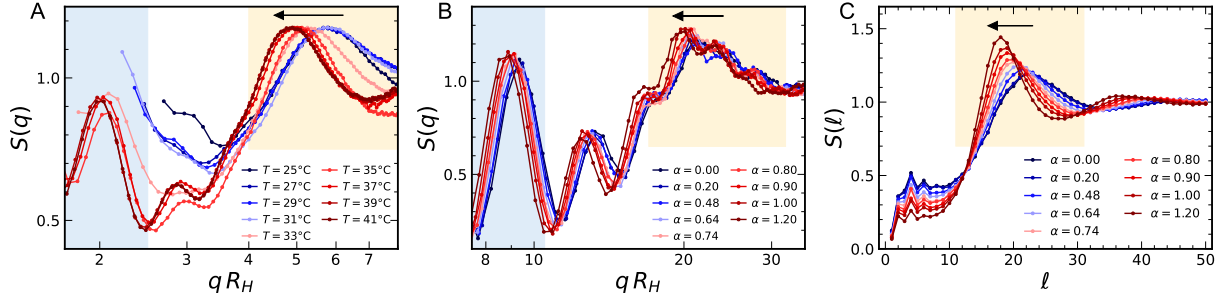


FIG. 2. Structural analysis of NPs adsorbed to microgels across the VPT: $S(q)$ as a function of qR_H for SAXS experiments (A) and numerical simulations (B). (C) spherical structure factors $S(\ell)$ of NPs from simulations for a microgel with $N = 14k$ and $f = 0.161$. In all panels, the shift towards lower q or ℓ is highlighted by a yellow region; in panel A, the curves are normalized to the maximum of same band to better visualize the shift.

complex across the VPT, occurring at $\alpha_C \sim 0.64$ (see also snapshots of Fig. 1C). We then calculate NP–NP structure factors, reported in Fig. 1D for $N = 112k$ and $n = 150$, which exhibit very similar features to experiments. Indeed, high oscillations at low q are followed by smaller peaks at intermediate q , showing overall a general shift of the peaks towards higher q with increasing temperature. However, the second peak, which in the simulations is around $0.2\sigma^{-1}$ (highlighted in light blue), is already present below the VPT, in contrast to experiments. This result is confirmed in all performed simulations, either varying f and NP number or modifying the microgel size (Fig. S5). Given that we do not detect specific NP structures, such as clusters or regular arrays, even if the peak is always present either at low or high effective temperatures, we conclude that its appearance in experiments may be the hallmark of more subtle structural modifications.

To shed light on the data, we move on to analyze the shift of all peaks towards large q values. To filter out the effect of the microgel deswelling due to the VPT, we plot $S(q)$ as a function of $qR_H(T)$ in Fig. 2A and B, for experiments and simulations, respectively, with $R_H(T)$ being the hydrodynamic radius at each temperature. In this way, it becomes evident that the region $qR_H \leq 2$, where the curves above the VPT have a peak, falls outside the experimental q -range below the VPT. Therefore, the peak should be already present at low temperatures, similarly to what found in simulations, but its apparent onset at high T is simply due to the fixed experimental q -window. Having established this, we take a closer look to Fig. 2 where, for both experimental and simulation data, the rescaled curves do not

perfectly overlap at different temperatures. Indeed, a shift towards lower q values is observed in both panels, pointing to a variation in NP-NP arrangement as a function of T . This effect needs to be appropriately interpreted within the spherical geometry constraint imposed on the NPs by the presence of the microgel. Hence, in order to decouple the contribution of the confining geometry to $S(q)$, we calculate the spherical structure factor $S(\ell)$ which is defined on the surface of a unit sphere as [15]

$$S(\ell) = 1 + \frac{2}{n} \sum_{(i,j)} P_\ell(\cos \gamma_{ij}) \quad (1)$$

where the sum is performed over all (i, j) NPs located at \vec{r}_i and \vec{r}_j , with $\gamma_{ij} = 2 \arcsin(\frac{1}{2}|\hat{r}_i - \hat{r}_j|)$ being the geodesic distance (angular distance on the unit sphere [15]) between the two NPs, \hat{r}_i the versor of \vec{r}_i and $P(\ell)$ is the Legendre polynomial of degree ℓ . Here, ℓ plays an equivalent role to the wave vector q in ordinary space, with the difference that it can only take discrete values since the spherical surface that defines the geometry has a finite size. The resulting $S(\ell)$ calculated at different temperatures in numerical simulations, for the representative case of a microgel with $N = 14k$ and $f = 0.161$, is shown in Fig. 2C, while the corresponding trend for a microgel with $N = 112k$ and $f = 0.02$ is reported in Fig. S6. The behavior of $S(\ell)$ is very similar to that of a standard structure factor in bulk, without all the low- q oscillations due to the underlying spherical geometry. We thus find that $S(\ell)$ is characterized by a main peak for $\ell \sim 18$, followed by smooth oscillations. The T -dependence of $S(\ell)$ shows that such main peak becomes sharper, shifting to lower and lower ℓ as T increases. Since this calculation is performed on a unit sphere, it is analogous to the rescaled $S(q)$ reported in Fig. 2B, thus confirming the shift observed in experiments and in simulations for the full structure factors. To sum up, the shift to low wavevectors of all structure factors clearly indicate that the NPs increase their relative geodesic distance (on the unit sphere) as the microgels undergo the VPT. This is due to their mutual electrostatic repulsion that becomes stronger and stronger as they get closer due to the underlying shrinking of the microgel. Furthermore, we note that the present data do not show evidence of a crystalline arrangement of NPs, although the degree of order increases due to the sharpening of the main peak in $S(\ell)$.

To connect the microscopic NP arrangement to the degree of plasmon coupling, we use a simple toy model, sketched in Fig. 3A and detailed in SM, which consists in randomly arranging a set of points, mimicking NPs, within a spherical shell, which represents the

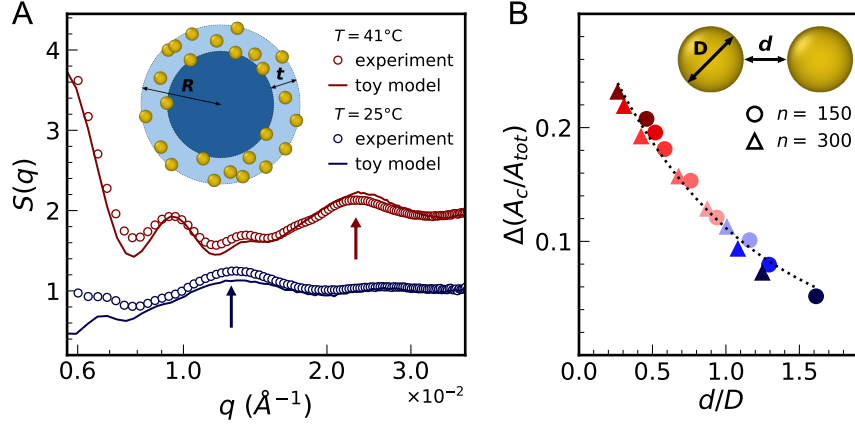


FIG. 3. (A) Experimental $S(q)$ compared to those obtained by a toy model (sketched in figure), using $N_p = 75$, $R = 184$ nm, $t = 47$ nm, $d_{min} = 28$ nm and $\sigma_R = 6$ nm for $T = 25^\circ\text{C}$, and $N_p = 65$, $R = 82$ nm, $t = 2$ nm, $d_{min} = 8$ nm, $\sigma_R = 6$ nm for $T = 41^\circ\text{C}$; the arrows identify the position of the peaks q_p corresponding to the distance between NPs. (B) Degree of coupling $\Delta(A_c/A_{tot})$ as a function of the parameter d/D , with d the surface-to-surface distance and $D = 18.6$ nm, being the NP diameter (Fig. S2), for $n = 150$ and $n = 300$; the dashed line is a fit to an exponential decay [34].

external corona of the microgels. By using this model, we are able to vary the features of the system arbitrarily, matching the experimental NP/microgel size ratio, which is not possible within the present simulations. In the toy model, we thus vary four different parameters independently: the external radius R and the thickness t of the shell, the number of NPs in the shell N_p and the minimum distance $D + d_{min}$ between them, where D is the NP diameter and d_{min} the minimum surface-to-surface distance. We then calculate $S(q)$ of the NPs within the shell and find that the model clearly allows us to interpret the different features of the measured $S(q)$ and to discern the influence of each parameter on its behavior (Figs. S7 and S8). Specifically, we confirm that the low- q features arise from the confinement of particles within a spherical shell, and indeed, they change when altering R and t . Instead, the broader band between 1 and $3 \times 10^{-2} \text{\AA}^{-1}$, whose maximum at q_p (highlighted by arrows) increases in intensity and shifts to higher q values with temperature, does not depend on the spherical geometry but rather on d_{min} and N_p . This band corresponds to the part of the experimental NPs structure factor that more strongly depends on their mutual interactions. Fig. 3A shows that, with an appropriate choice of parameters, and accounting for the experimental

polydispersity σ_R as detailed in the SM, it is possible to almost quantitatively reproduce the experimental spectra, in particular matching the position of the various peaks of the experimental $S(q)$. Despite minor deviations in the intensities of the maxima and minima at low q , due to the underlying simplicity of the model, we conclude from this analysis that the more pronounced peaks occurring at intermediate q in experiments are due to the uniforming of the core-corona structure of the microgels as they undergo the VPT. Notably, the model yields meaningful values of the parameters for the description of the experimental results and their trend with temperature. Indeed, we find that the external radius of the shell R shrinks from 184 to 82 nm, in good agreement with R_H measurements reported in Fig. S3, while the shell thickness t reduces from 47 to 2 nm. This pronounced shrinking of the shell, much greater than the overall microgel deswelling, is due to the incorporation of NPs [32], indicating that, across the VPT, the corona of the microgel compacts much more than the core, thus pushing the NPs outward. The further action of mutual electrostatics finally results in the rearrangement of NPs at overall larger relative distances, also favouring an increase ordering, as revealed by $S(\ell)$.

Based on these results, we are finally able to connect the experimental $S(q)$ with the optical properties of the complexes as the microgels undergo the VPT. Starting from the position q_p of the first peak attributable to the effective structure factor of NPs (see Fig. 3A), we determine the average surface-to-surface distance $d = 2\pi/q_p - D$ between nearest neighbors and plot the degree of coupling, obtained from the extinction spectrum at the same T , against the parameter d/D to quantify the interaction strength [34] (Fig. 3B). Since NPs approach each other more and more closely upon shrinking of the microgels above the VPT, they are able to explore distances of just a few nanometers between their gold surfaces, suitable to give rise to plasmon coupling. Notably, we find that the trends for the two studied values of n follow the same exponential decay pattern [34], with a decay length of ~ 20 nm. This evidences for the first time a direct relationship between the coupling of plasmonic NPs adsorbed onto thermoresponsive microgels and their average inter-particle distance. This enables the optical measurement of the NP-NP nanoscale distances on the spherical surface as a function of temperature, thus serving as a plasmonic “nano-ruler”, similar to those based on DNA technology [35].

In summary, the present work represents the first microscopic analysis of the spatial organization of plasmonic NPs electrostatically adsorbed on thermoresponsive microgels and

of its modifications across the VPT. By combining SAXS and numerical simulations, supported by a simple toy model, we have unambiguously identified the many complex features occurring in the $S(q)$ of the NPs, interpreting their modifications as a function of temperature. Our analysis reveals that, besides the expected rescaling of NP–NP distances due to the microgel collapse, subtle changes occur in their relative arrangement. In particular, we detect a tendency of the NPs to increase their relative distance on the spherical surface of the microgel due to their underlying electrostatic repulsion. This effect is enhanced by the narrowing of the outer shell, that is more intense than the corresponding deswelling of the whole microgel, forcing the NPs to position more externally. The interplay of these mechanisms induces the NPs to arrange in increasingly ordered structures, as evidenced by the increase of the intensity of the spherical structure factor with temperature, albeit without reaching a crystalline arrangement. Most importantly, we establish a link between the structure of the microgel–NPs complexes and their optical properties, providing evidence of the relationship between the degree of plasmon coupling in the extinction spectra and the surface-to-surface distance between neighbor NPs. Additionally, we demonstrate that plasmonic NPs, besides their use for a wide range of applications, can serve as local optical probes to extract microscopic information on the structure of ionic microgels and act as a thermal plasmon ruler where the macroscopic response strictly depends on the NPs organization, driven by the microgel shrinking across the VPT. This opens the way to a rational design of thermoresponsive plasmonic systems with adjustable optical properties tailored to specific needs.

We acknowledge SOLEIL for providing synchrotron radiation facilities under proposal n. 20191601 at the SWING beamline and CINECA-ISCRA for HPC resources. F.Br., F. B., E.Z. and S.S. acknowledge financial support from INAIL, project MicroMet (BRiC 2022, ID 16). A.C. acknowledges financial support from the European Union - NextGenerationEU under the Italian Ministry of University and Research (MUR) National Innovation Ecosystem grant ECS00000041 - VITALITY - CUP E13C22001060006. D.T. and E.C. acknowledge financial support from the Agence Nationale de la Recherche (Grant ANR-20-CE06-0030-01; THELECTRA). We thank A.L. Božič for valuable discussion.

SUPPLEMENTAL MATERIAL

S1. EXPERIMENTAL METHODS

Microgel synthesis. Our experiments are performed on cationic microgels with fraction of crosslinker monomer $c = 0.05$ and of initiator $f/2 = 0.01$, synthesized by the surfactant-free radical polymerization previously detailed [32, 36]. We dissolve 1.25 g of NIPAM monomers (Sigma-Aldrich, MW = 113.16 Da) and the crosslinker N,N'-methylene-bis-acrylamide (BIS, Sigma-Aldrich, MW = 154.17 Da) in 148 mL of deionized water. Separately, the ionic initiator 2,2'-Azobis(2-methylpropionamidine) dihydrochloride (AIBA, Sigma-Aldrich, MW = 271.19 Da) is dissolved in 2 mL of water. The solution containing NIPAM and BIS is bubbled with argon for 30 minutes and, after heating up to 70 °C, the initiator solution is added. At 70°C, AIBA undergoes homolytic cleavage forming two radicals, each including one amine group. Each radical reacts with a NIPAM monomer and produces a new radical, giving rise to the polymerization reaction. Therefore, after starting the reaction, amines of AIBA initiator remain attached to the backbone of the microgels, providing them positive charge due to protonation. After 6-hour reaction, the obtained dispersion is cooled down to room temperature and filtered through glass wool. To prevent bacterial growth, NaN_3 (Sigma-Aldrich, MW = 65.01 Da) is added to the concentration of 2 mM. The hydrodynamic radius of the microgels, measured by dynamic light scattering (DLS) at 25°C, is $R_H = 286$ nm. The final number density of the microgels in the dispersion is evaluated to $n_{mg} = 1.63 \times 10^{12} \text{ mL}^{-1}$ by viscosimetry measurements as described in Refs. 32 and 37.

Preparation of microgel-nanoparticles samples. We use spherical gold nanoparticles (NPs, Ted Pella) with nominal diameter $D = 20$ nm and number density $n_{NP} = 7.0 \times 10^{11} \text{ mL}^{-1}$. A stabilizing citrate capping provides NPs with a negative charge, previously evaluated to $q_{NP} = -35 e$ [32]. The very low concentration guarantees that possible effects on the ionic strength of the final samples due to ions release from the NPs surface are negligible. To prepare samples, we dilute separately the microgel dispersion 250 times in 0.4 mM NaN_3 and the NPs one in water to obtain the desired number ratio $n = n_{NP}/n_{mg}$. We then mix the two components and gently agitate the solution by hand. The concentration of NaN_3 in the final samples is 0.2 mM, low enough to exclude any effect of the ionic strength on the

microgel swelling.

Since we are interested in studying the plasmon coupling, that takes place for surface-to-surface distances between NPs of few nanometers, we choose high n values to achieve sufficiently small distances and to avoid inducing aggregation of the microgel–NPs complexes. Preliminary DLS and extinction spectroscopy experiments show that these conditions are matched for $n \geq 100$. Moreover, since for high n only part of the NPs in the sample is actually incorporated within the microgel network due to the electrostatic repulsion [32], we need to ensure that the portion of non-adsorbed NPs is not predominant to avoid compromising the outcomes of the experiments. A previous study of NPs adsorption on microgels with $f = 0.032$ [32] shows that this requirement is well-fulfilled for $n \leq 300$. Even though the microgels in this study are slightly less charged, we adhered to these limits, selecting $n = 150$ and $n = 300$. This choice is further supported by the fact that we were able to acquire extinction and scattering intensity spectra with a good signal, suitable for the analyses of this study.

Extinction spectroscopy. Extinction spectra in the UV–Visible–NIR spectral range were acquired by including the samples in a 1 mm quartz cuvette and using a v-570 double ray spectrophotometer (Jasco, Tokyo, Japan), equipped with a Peltier thermostatted holder EHC-505 (Jasco). The instrument has a spectral resolution of 0.1 nm in the UV–Visible range and 0.5 nm in the NIR range. For measurements at varying temperature, samples were kept thermalising 5 minutes after every temperature change before acquisition. All the spectra reported in the figures are normalized to the extinction at 400 nm, that corresponds to the onset of the gold interband transitions and is unaffected by particle size, shape, and environment, contrarily to the LSPR [14].

Small Angle X-ray Scattering. For Small Angle X-ray Scattering (SAXS) experiments, samples were filled in capillaries (1.5 mm diameter) and placed at the sample-to-detector distance of 3 m. The exposure time for acquisitions was set to 1 s and 14 scattering patterns were acquired for each sample. Scattering patterns were recorded at 12 keV using a two-dimensional EigerX 4-M detector (Dectris, Baden, Switzerland). This allows measurements in the range of q -vector between 0.002 and 0.38 \AA^{-1} , where q is defined as $q = (4\pi/\lambda) \sin \theta$, 2θ is the scattering angle, and λ is the wavelength of the radiation. Scattering patterns of an empty capillary and of a capillary filled with water were recorded for normalization of the intensity to absolute units and background subtraction, respectively. Experiments

were conducted at selected temperatures between 25 and 41 °C employing a Huber Mini-stat 125 thermostat. After each temperature change, samples were left thermalizing for 5 minutes before measurements. The processing and averaging of the scattering patterns were performed by the software Foxtrot (SOLEIL software group and SWING beamline). When averaging, any scattering curve not perfectly superimposed with the overall set acquired, due to possible residual equilibration or other experimental perturbations, was discarded.

For a collection of particles, the scattered intensity $I(q)$ can be expressed in terms of the form factor $P(q)$ of single particles and of the structure factor $S(q)$ of the system as $I(q) = nv^2\Delta\rho^2P(q)S(q)$, where n and v are the number density and the volume of the scattering particles, and $\Delta\rho$ is the contrast in electron density between particles and solvent. Since for a dilute system of non-interacting scatterers $S(q) = 1$, we directly measured the form factor of gold NPs on the stock solution [24]. In microgel–NPs samples, given the extremely higher contrast $\Delta\rho$ of gold than that of the polymer chains, it is reasonable to assume that the measured scattered intensities, with the chosen acquisition times, originates solely from the NPs present in the sample. We verified this assumption by measuring a microgel sample without NPs in the same experimental conditions, resulting in almost null scattered intensity. We therefore could simply derive the structure factor of NPs by dividing the scattered intensity measured on each sample by the form factor of NPs.

Dynamic Light Scattering. Size distributions in terms of hydrodynamic radius R_H were measured by Dynamic Light Scattering (DLS), employing a NanoZetaSizer apparatus (Malvern Instruments LTD) equipped with a He–Ne laser (5 mW power, 633 nm wavelength) that collects light in quasi-backscattering geometry, at an angle of 173°. Decay times, extrapolated from the acquired intensity autocorrelation functions, are used to determine the distribution of diffusion coefficients D_T of the particles. Diffusion coefficients are then converted to intensity-weighted distributions of R_H using the Stokes-Einstein relationship $R_H = k_B T / 6\pi\eta D_T$, where $k_B T$ is the thermal energy and η the water viscosity. Temperature trends are measured using ascending ramps between 25 °C and 41 °C. After each temperature variation, the samples were kept thermalizing for 5 minutes before performing the measure. Each value of R_H reported in the work is the average of a distribution obtained by at least 50 measurements. The associated error is the corresponding standard deviation.

S2. ADDITIONAL EXPERIMENTS

Optical analysis: extinction spectra and plasmon coupling. We report in Fig. S1 the extinction spectra of the NPs stock dispersion, which due to its high dilution and colloidal stability ensures that there is no plasmon coupling, and of microgel–NPs complexes as a function of temperature between 25°C and 41°C, for the number ratios $n = 15$ and $n = 300$. At the smaller n , the NPs remain far apart even above the VPT, therefore no plasmon coupling is observed and the maximum shift of the LSPR, of 8 nm, can be attributed solely to the variation of refractive index at the interface of the NPs, caused by water expulsion from the polymer network and chain densification. At larger n values, the maximum shift is higher, reaching 10 nm for $n = 150$ and 16 nm for $n = 300$. However, even if the shift of the LSPR gives a good description of the optical changes across the VPT, it does not reveal any information about broadening of the peak and onset of coupled plasmon modes at higher wavelengths, that are the main features of interest for many applications, such as colorimetric detection or surface-enhanced spectroscopies [27]. To account for these changes, clearly distinguishable in the spectra, we therefore choose a more robust method to quantify the plasmon coupling. Analogously to refs. 27 and 28, we identify the spectral region of coupled modes in the wavelength range from 570 to 800 nm (inset of Fig. 1A), where only low-energy modes resulting from near-field interactions contribute to the extinction, and calculate their spectral weight. We then define the coupling degree as

$$\Delta \frac{A_C}{A_{tot}} = \frac{A_C(T)}{A_{tot}(T)} - \frac{A_C^{(NP)}}{A_{tot}^{(NP)}} \quad (\text{S1})$$

where $A_{tot}(T)$ and $A_C(T)$ are the areas underlying the spectrum acquired at temperature T on the microgel–NPs samples, in the overall spectral range and in the region of coupled modes, respectively; $A_{tot}^{(NP)}$ and $A_C^{(NP)}$ are the corresponding areas computed from the reference spectrum of NPs stock dispersion, which due to its high dilution and colloidal stability ensures the absence of plasmon coupling.

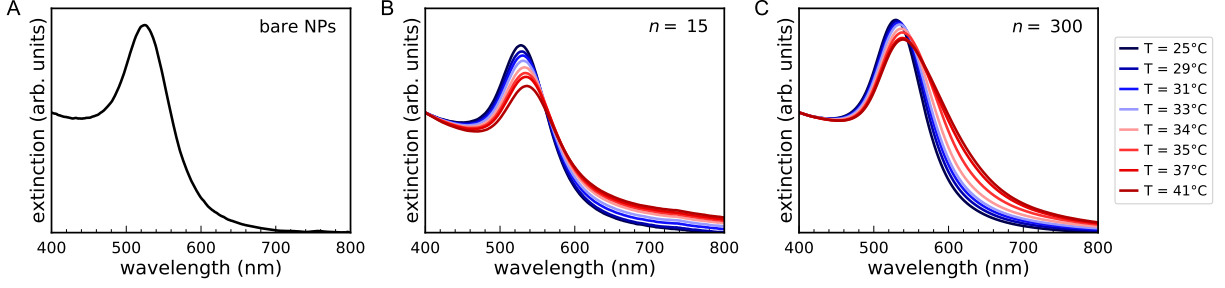


FIG. S1. Extinction spectra of the NPs stock dispersion (A) and of the microgel–NPs complexes as a function of temperature for $n = 15$ (B) and $n = 300$ (C).

SAXS analysis: form factor of gold NPs and structure factors of microgel–NPs. The form factor of gold NPs is directly measured by SAXS on dilute samples, with number density $n_{NP} = 7.0 \times 10^{11} \text{ mL}^{-1}$. The acquired scattering curve is reported in Fig. S2A. We fitted the curve to a spherical form factor model [38] with log-normal particle size distribution, to evaluate the radius of NPs to 9.3 nm with 10% polydispersity. The good overlap between the two curves also ensures the validity of the assumption that there is no interaction between the dispersed NPs, thus the scattering curve represents their form factor.

In Fig. S2B, we report the structure factors of NPs measured on microgel–NPs samples with with number ratio $n = 300$ as a function of temperature between 25°C and 41°C.

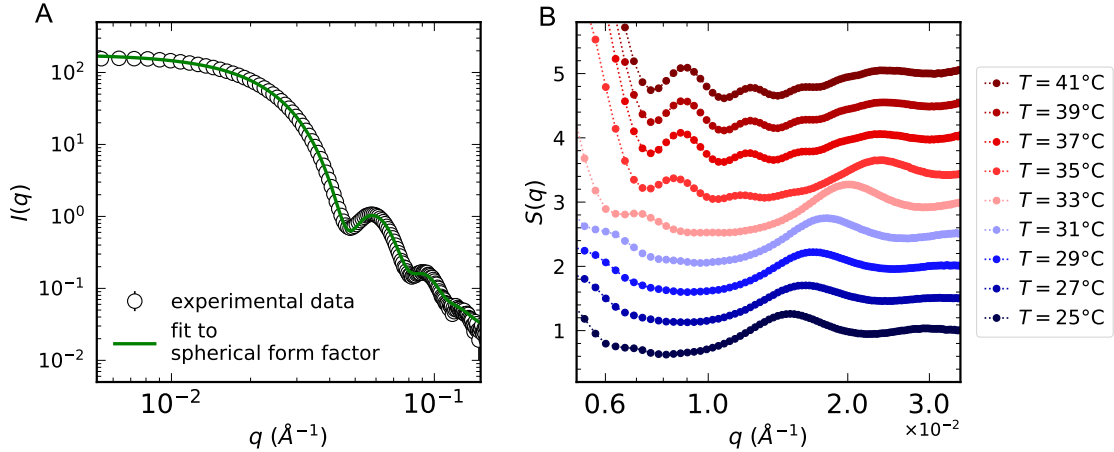


FIG. S2. (A) Experimental form factor of gold NPs and best fit to a sphere model. (B) Structure factors of NPs as a function of temperature for the microgel–NPs sample with $n = 300$.

Swelling curves of microgels. The experimental swelling curve of the microgels, obtained plotting R_H as a function of temperature is reported in Fig. S3. Based on it, we extrapolated the transition temperature $T_C = 33.3 \pm 0.3$ °C, by fitting data to the sigmoidal-like function

$$y = y_\infty + \frac{y_0 - y_\infty}{1 + e^{\frac{x - T_C}{\Delta T}}} \quad . \quad (\text{S2})$$

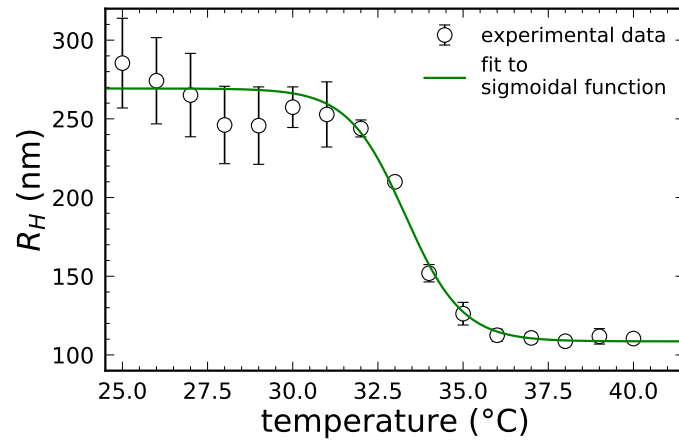


FIG. S3. Swelling curve of the microgel and best fit to a sigmoidal-like function.

S3. NUMERICAL SIMULATIONS

Modelling microgel-NPs. We use coarse-grained microgels consisting of fully-bonded, disordered polymer networks of N spherical beads with diameter σ and mass m , which set the length and mass units. Nanoparticles are also spherical beads of diameter D and mass m .

Microgels of $N = 112k$ or $N = 14k$ monomers are prepared with the protocol previously reported in Refs. 29 and 30, which was found to reproduce very well the experimental structure of the particles. After assembly, monomers interact via the bead-spring model, established by Grest and Kremer [39], which amounts to the sum of a steric repulsion for all beads plus a bond term for the connected ones. The first term is modelled by the Weeks–Chandler–Anderson (WCA) potential:

$$V_{\text{WCA}}(r) = \begin{cases} 4\varepsilon \left[\left(\frac{\sigma}{r}\right)^{12} - \left(\frac{\sigma}{r}\right)^6 \right] + \varepsilon & \text{if } r \leq 2^{1/6}\sigma \\ 0 & \text{if } r > 2^{1/6}\sigma \end{cases} \quad (\text{S3})$$

where r is the center-to-center distance between a given pair of interacting particles and ε sets the energy scale. In addition, bonded monomers interact via the Finitely Extensible Nonlinear Elastic (FENE) potential [31, 40]:

$$V_{\text{FENE}}(r) = -\epsilon k_F R_F^2 \ln \left[1 - \left(\frac{r}{R_F \sigma} \right)^2 \right], \quad r < R_F \sigma \quad (\text{S4})$$

with $R_F = 1.5$ and $k_F = 15$. Monomers are linked via the FENE potential to two neighbours representing segments of NIPAM chains, whereas crosslinkers have a fourfold valence. As for experiments, we use the molar fraction of crosslinker $c = 0.05$ and bonds, once assembled, cannot break during the course of a simulation.

To model the VPT of microgels, we introduce an effective solvophobic potential V_α , acting only between divalent monomers, which implicitly accounts for monomer–solvent interactions [33]:

$$V_\alpha(r) = \begin{cases} -\varepsilon \alpha & \text{if } r \leq 2^{\frac{1}{6}}\sigma \\ \frac{1}{2} \alpha \varepsilon [\cos(\gamma_0(r\sigma)^2 + \beta_0) - 1] & \text{if } 2^{\frac{1}{6}}\sigma < r \leq R_F \sigma \\ 0 & \text{if } r > R_F \sigma \end{cases} \quad (\text{S5})$$

where $\gamma_0 = \pi(2.25 - 2^{1/3})^{-1}$ and $\beta_0 = 2\pi - 2.25\gamma_0$. This term represents an effective attraction, modulated by the solvophobic parameter α , which plays the role of an effective temperature. Therefore, $\alpha = 0$ represents good solvent conditions (at low temperature, below the transition), while as α rises, the attraction between monomers grows, leading to aggregation and microgel shrinkage; the overall behavior echoing the worsening of the monomer affinity to the solvent when temperature is risen [29, 41].

To mimic the ionic groups of AIBA monomers, we provide a fraction f of the microgel beads with a positive charge. Similar to experiments, we simulate microgels with surface charge distribution, where we assign charged beads randomly, but only in the exterior corona of the microgel, i.e. where the distance from the microgel centre of mass is higher than R_g . To ensure the overall electro-neutrality, for each charged monomer we also insert an oppositely charged counterion, whose diameter is set to $\sigma_c = 0.1\sigma$ [31]. Counterions interact among each other and with microgel beads through the WCA potential. Additionally, all charged particles interact with the Coulomb potential:

$$V_{\text{coul}}(r_{ij}) = \frac{q_i q_j \sigma}{e^* r_{ij}} \varepsilon, \quad (\text{S6})$$

where q_i and q_j are the charges of the interacting beads ($+e^*$ for charged monomers of the microgel and $-e^*$ for counterions), being $e^* = \sqrt{4\pi\epsilon_0\epsilon_r\sigma}\varepsilon$ the reduced charge unit and ϵ_0 , ϵ_r the vacuum and relative dielectric constants, respectively. The particle-particle-particle-mesh method [42] is adopted to appropriately account for the long-range nature of the Coulomb interactions. Following our previous works [43, 44], charged monomers on the microgel do not interact with the solvophobic potential, even when temperature increases, to ensure their maintained hydrophilic character in the whole investigated temperature range.

Finally, NPs are represented as single beads with negative charge $q = -35e^*$ of diameter D . To maintain the same proportion between NPs and microgel sizes as in the experiments, we use two values of the diameter, $D = 4\sigma$ for microgels with $N = 112k$ and $D = 2\sigma$ for $N = 14k$. Similarly to when assigning charge to AIBA monomers, an appropriate number of positive counterions ($q = +e^*$, $\sigma_c = 0.1\sigma$) are added to preserve for all studied conditions the overall neutrality of the system. NPs, as all charged beads, interact among each other and with all other beads through the WCA and Coulomb potentials. For all mixed interactions, the interaction lengths are given by the mixed diameters $\sigma_{ab} = (\sigma_a + \sigma_b)/2$, with a, b indicating all different species involved (NPs, monomers either charged or uncharged and

all counterions).

NVT simulations are performed with the LAMMPS package [45] at the temperature fixed by $k_B T = \varepsilon$ in a cubic box with side L and periodic boundary conditions. We choose $L = 600 \sigma$ for $N = 112000$ and $L = 300 \sigma$ for $N = 14000$. The equations of motion are integrated with a time-step $\Delta t = 0.002 \tau$, where $\tau = \sqrt{m\sigma^2/\varepsilon}$ is the reduced time unit. We use the Nosé-Hoover thermostat in the constant NVT ensemble for equilibration (1000τ) and the Velocity-Verlet algorithm in the constant-energy ensemble for the production runs (20000τ). The latter are used to extract the equilibrium averages of the observables of interest.

The size of microgel–NPs complexes is characterized in terms of hydrodynamic radius R_H , computed from simulations using the ZENO software [46]. We include in the calculation all the monomers of the microgel and all NPs bound to charged monomers, identified as those with distance from the closest charged monomer is lower than $1.25(D + \sigma)$.

The structure factors of adsorbed NPs are calculated at each wavenumber q as:

$$S(q) = \frac{1}{N_{\text{ads}}} \sum_{i=1}^{N_{\text{ads}}} \sum_{j=1}^{N_{\text{ads}}} e^{-i\vec{q}\cdot\vec{r}_{ij}} \quad , \quad (\text{S7})$$

where \vec{r}_{ij} is the distance between the i -th and j -th NPs, and the sum is performed over all the N_{ads} NPs adsorbed to the microgel, identified as those whose distance from the microgel center of mass is lower than $R_H + D/2$.

The spherical structure factors $S(\ell)$ are calculated using the geodesic distances between the NPs, *i.e.* the angle determined by their positions on the unit spherical surface centered at the microgel's center of mass. For an (i, j) pair of NPs, located at \vec{r}_i and \vec{r}_j , the geodesic distance γ_{ij} is given by:

$$\gamma_{ij} = 2 \arcsin\left(\frac{1}{2}|\hat{r}_i - \hat{r}_j|\right) \quad , \quad (\text{S8})$$

where $\hat{r}_{i/j}$ is the versor of $\vec{r}_{i/j}$. $S(\ell)$ is then defined as [15]:

$$S(\ell) = 1 + \frac{2}{n} \sum_{(i,j)} P_\ell(\cos \gamma_{ij}) \quad , \quad (\text{S9})$$

where the sum is performed over all (i, j) pairs and $P(\ell)$ is the Legendre polynomial of degree ℓ . Here, ℓ plays an equivalent role to the wave vector q in ordinary space, with the difference that it can only take discrete values since the spherical surface that defines the geometry has a finite size.

Swelling curve. The swelling curve of the simulated microgel for $N = 112k$ and $f = 0.02$, as obtained by plotting R_H as a function of α is reported in Fig. S4. Based on it, we extrapolate the equivalent transition temperature $\alpha = 0.64 \pm 0.01$, fitting the data to the sigmoidal-like function of Eq. S2.

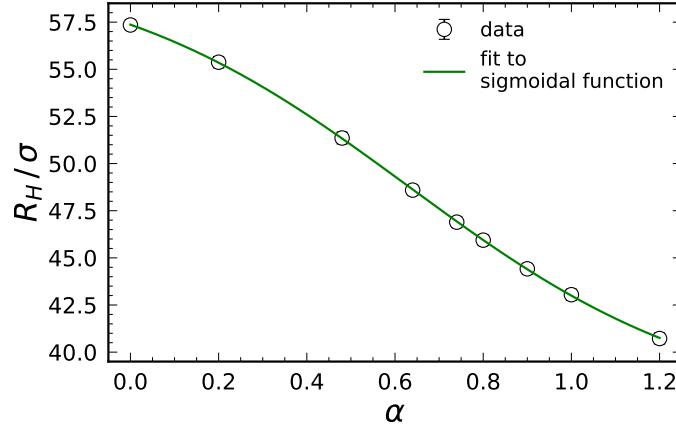


FIG. S4. Swelling curve, R_H as a function of α , of the microgel, where the microgel ($N = 112k$ and $f = 0.02$) interacts with $n = 150$ NPs, and best fit to a sigmoidal-like function.

Structure factors of NPs adsorbed to microgels. The NPs structure factors for the microgels with $N = 112k$ and $f = 0.02$ at different NP/microgel number ratios and for different microgel compositions ($N = 14k$ and $f = 0.02$, $N = 14k$ and $f = 0.16$, $N = 112k$ and $f = 0.01$) at fixed $n = 150$ are reported as a function of α in figure Fig. S5. In all the cases considered, the high oscillations at low q are followed by smaller peaks at intermediate q (highlighted in light blue). These peaks are present for all the effective temperature, in contrast to experiments.

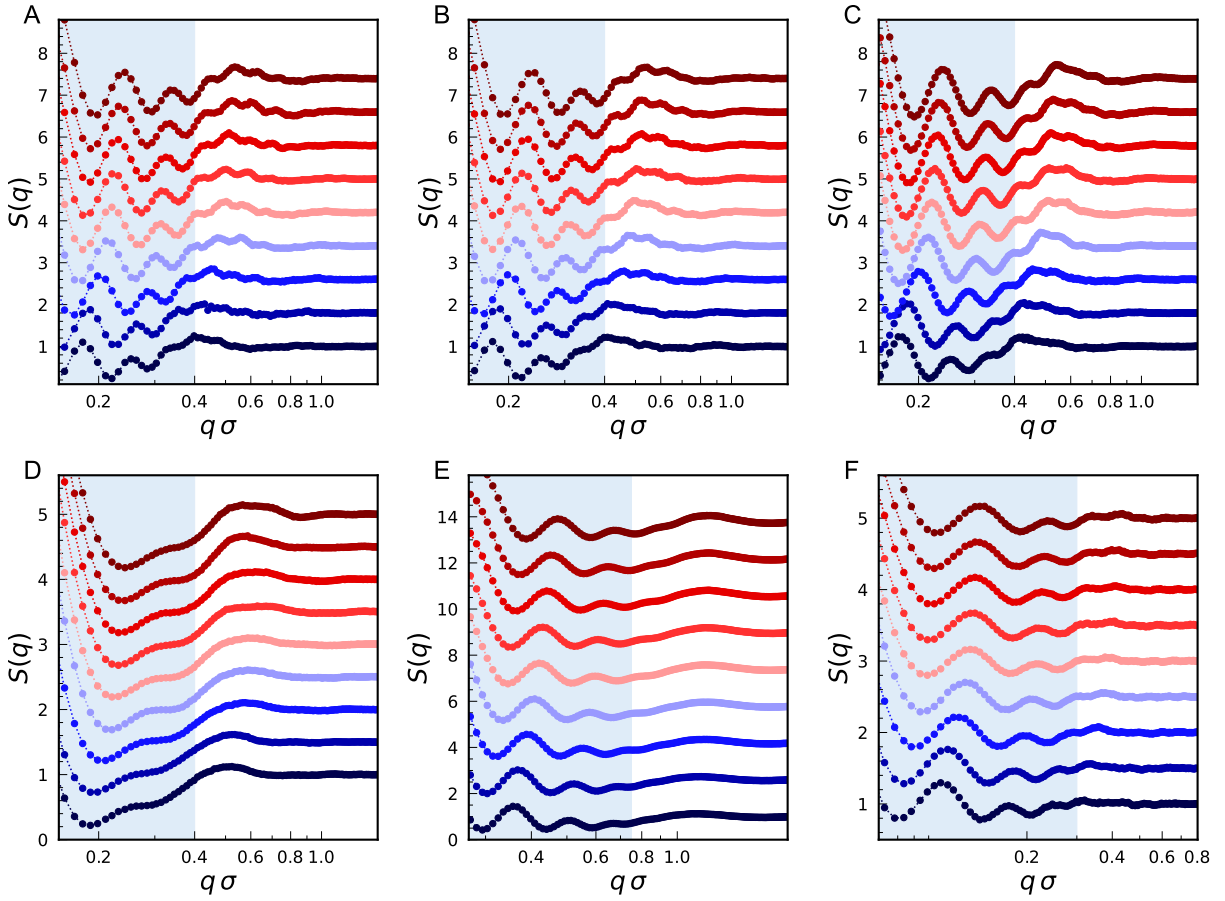


FIG. S5. Structure factors at varying α for different microgel–NPs systems: microgel with $N = 112k$ and $f = 0.02$, for $n = 80$ (A), $n = 100$ (B) and $n = 300$ (C), and microgels with $N = 14k$ and $f = 0.02$ (D), $N = 14k$ and $f = 0.16$ (E), $N = 112k$ and $f = 0.01$ (F) at fixed $n = 150$.

Spherical structure factors of NPs adsorbed to microgels. The spherical structure factors of the adsorbed NPs for the system with $N = 112k$, $f = 0.02$ and $n = 150$, computed according to Eq. S9, are reported as a function of α in figure Fig. S6. We find that $S(\ell)$ is characterized by a main peak for $\ell \sim 16$, followed by smooth oscillations. Additionally, it approaches a low value as $\ell \rightarrow 0$. The T -dependence of $S(\ell)$ shows that the main peak becomes sharper, shifting to lower ℓ as T increases. The same variations are more pronounced in the case of the microgel with $N = 112k$ and $f = 0.16$ reported in Fig. 2C. To sum up, the shift to low wavevectors of all structure factors clearly indicate that the NPs increase their relative (geodesic) distance as the microgels undergo the VPT.

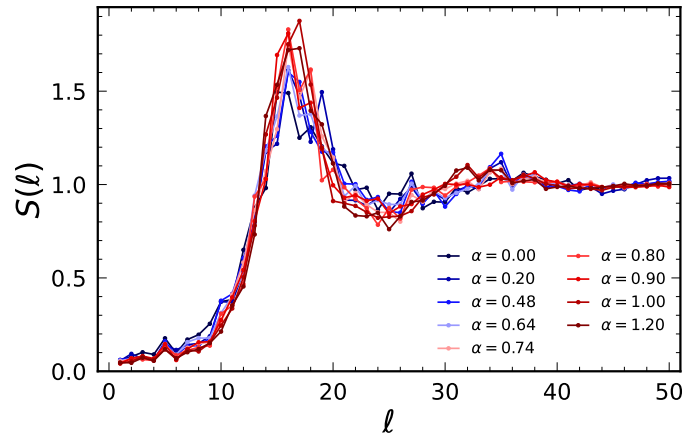


FIG. S6. Spherical structure factors at varying α for the microgel–NPs complex with $N = 112k$, $f = 0.02$ and $n = 150$.

S4. TOY MODEL

Description of the model The toy model, sketched in Fig. 3A, consists in a set of particles randomly positioned within a spherical shell; the particles mimic the NPs and the shell they are restrained represents the external corona of the microgel. The system is built from four parameters: the external radius R of the shell, its thickness t , the desired number N_p of particles to be placed within the shell and the minimum surface-to-surface distance d_{min} between any two particles. The procedure to place the i th particle inside the shell is the following: first, (i) a random position within the shell is generated; next, (ii) the distance of this newly created position to all $i - 1$ previously inserted particles is calculated; (iii) if the distance is larger than $D + d_{min}$ for all present particles (here $D = 18.6$ nm is the NP diameter, obtained by the fit of Fig. S2), the i th particle is assign to this position. The procedure is repeated in case of failing to allocate a new particle for a maximum number of $50k$ attempts for each of the N_p desired particles. The limiting maximum number of attempts imply that systems with high surface densities may contain less particles than the N_p desired one.

For each set of the four parameters, we prepare 100 distinct configurations and compute the average of the corresponding structure factors, according to Eq. S7. To account for size polydispersity of experimental microgels, we consider a Gaussian distribution for the shell radius, defined by the mean value R_0 and standard deviation σ_R . We then extract from the distribution a different value of R for each of the 100 configurations; to keep constant the geometrical proportions, the shell thickness is also corrected by a factor R/R_0 . In this way the features of the average structure factor result more smoothed and therefore overlap better with experimental data.

We used the toy model to achieve a full comprehension of the structure factors of the NPs adsorbed to microgel. Specifically, we varied each of the model parameters independently to understand how it affects the features of the $S(q)$. The trends at varying the shell parameters R_0 , t and σ_R are shown in Fig. S7, those at varying the NPs parameters N_p and d_{min} are shown in Fig. S8.

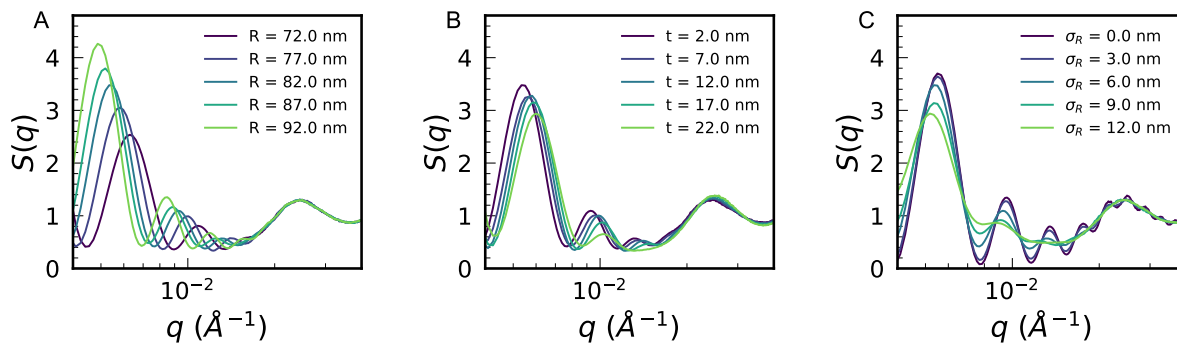


FIG. S7. Structure factors of the toy model, consisting in particles with random positions within a spherical shell, at varying independently each geometrical parameter of the shell R (A), t (B) and σ_R (C). The following values are used for the parameters that are kept constant: $R = 82$ nm, $t = 2$ nm, $\sigma = 6$ nm, $N_p = 150$ and $d_{min} = 8$ nm.

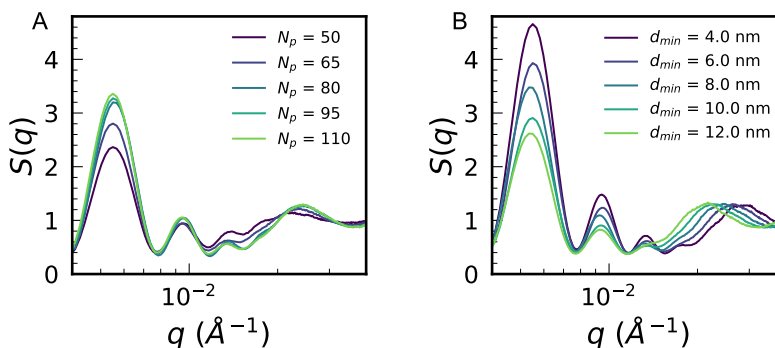


FIG. S8. Structure factors of the toy model, consisting in particles with random positions within a spherical shell, at varying independently each parameter of the NPs, N_p (A) and d_{min} (B). The following values are used for the parameters that are kept constant: $R = 82$ nm, $t = 2$ nm, $\sigma = 6$ nm, $N_p = 150$ and $d_{min} = 8$ nm.

-
- [1] L. A. Lyon and A. Fernandez-Nieves, Annual review of physical chemistry **63**, 25 (2012).
 - [2] M. Karg and T. Hellweg, Current Opinion in Colloid & Interface Science **14**, 438 (2009).
 - [3] A. Fernandez-Nieves, H. Wyss, J. Mattsson, and D. A. Weitz, *Microgel Suspensions: Fundamentals and Applications* (John Wiley & Sons, 2011).

- [4] D. Suzuki, *Langmuir* **39**, 7525 (2023).
- [5] A. Scotti, M. F. Schulte, C. G. Lopez, J. J. Crassous, S. Bochenek, and W. Richtering, *Chemical reviews* **122**, 11675 (2022).
- [6] L. Rovigatti, N. Gnan, L. Tavagnacco, A. J. Moreno, and E. Zaccarelli, *Soft matter* **15**, 1108 (2019).
- [7] D. Suzuki, Y. Nagase, T. Kureha, and T. Sato, *The Journal of Physical Chemistry B* **118**, 2194 (2014).
- [8] A. Choe, J. Yeom, R. Shanker, M. P. Kim, S. Kang, and H. Ko, *NPG Asia Materials* **10**, 912 (2018).
- [9] V. Sabadasch, L. Wiehemeier, T. Kottke, and T. Hellweg, *Soft Matter* **16**, 5422 (2020).
- [10] M. Arif, Z. H. Farooqi, A. Irfan, and R. Begum, *Journal of Molecular Liquids* **336**, 116270 (2021).
- [11] F. Diehl, S. Hageneder, S. Fossati, S. K. Auer, J. Dostalek, and U. Jonas, *Chemical Society Reviews* **51**, 3926 (2022).
- [12] Z. Ye, C. Chen, L. Cao, Z. Cai, C. Xu, H.-I. Kim, J. P. Giraldo, A. G. Kanaras, and Y. Yin, *Angewandte Chemie International Edition* , e202408020 (2024).
- [13] K. Gawlitza, S. T. Turner, F. Polzer, S. Wellert, M. Karg, P. Mulvaney, and R. von Klitzing, *Physical Chemistry Chemical Physics* **15**, 15623 (2013).
- [14] V. Amendola, R. Pilot, M. Frascioni, O. M. Maragò, and M. A. Iatì, *Journal of Physics: Condensed Matter* **29**, 203002 (2017).
- [15] A. L. Božič and S. Čopar, *Physical Review E* **99**, 032601 (2019).
- [16] A. G. Meyra, G. J. Zarragoicochea, A. L. Maltz, E. Lomba, and S. Torquato, *Physical Review E* **100**, 022107 (2019).
- [17] L. N. Carenza, G. Gonnella, D. Marenduzzo, G. Negro, and E. Orlandini, *Physical Review Letters* **128**, 027801 (2022).
- [18] P. Viveros-Méndez, J. Méndez-Alcaraz, and P. González-Mozuelos, *The Journal of Chemical Physics* **128**, 10.1063/1.2816558 (2008).
- [19] N. Singh, A. Sood, and R. Ganapathy, *Nature Communications* **11**, 4967 (2020).
- [20] L. Javidpour, A. Božič, A. Naji, and R. Podgornik, *Soft Matter* **17**, 4296 (2021).
- [21] N. J. Halas, S. Lal, W.-S. Chang, S. Link, and P. Nordlander, *Chemical reviews* **111**, 3913 (2011).

- [22] K. Zygadlo, C.-H. Liu, E. R. Bernardo, H. Ai, M.-P. Nieh, and L. A. Hanson, *Nanoscale Advances* **6**, 146 (2024).
- [23] Z. Li, W. Wang, and Y. Yin, *Trends in Chemistry* **2**, 593 (2020).
- [24] A. Capocéfalo, T. Bizien, S. Sennato, N. Ghofraniha, F. Bordi, and F. Brasili, *Nanomaterials* **12**, 1529 (2022).
- [25] H. Liu, Z. Yang, L. Meng, Y. Sun, J. Wang, L. Yang, J. Liu, and Z. Tian, *Journal of the American Chemical Society* **136**, 5332 (2014).
- [26] D. Caprara, F. Ripanti, A. Capocéfalo, A. Sarra, F. Brasili, C. Petrillo, C. Fasolato, and P. Postorino, *Colloids and Surfaces A: Physicochemical and Engineering Aspects* **589**, 124399 (2020).
- [27] D. Aili, P. Gryko, B. Sepulveda, J. A. Dick, N. Kirby, R. Heenan, L. Baltzer, B. Liedberg, M. P. Ryan, and M. M. Stevens, *Nano letters* **11**, 5564 (2011).
- [28] M. H. Chowdhury, A. M. Julian, C. J. Coates, and G. L. Coté, *Journal of Biomedical Optics* **9**, 1347 (2004).
- [29] N. Gnan, L. Rovigatti, M. Bergman, and E. Zaccarelli, *Macromolecules* **50**, 8777 (2017).
- [30] A. Ninarello, J. J. Crassous, D. Paloli, F. Camerin, N. Gnan, L. Rovigatti, P. Schurtenberger, and E. Zaccarelli, *Macromolecules* **52**, 7584 (2019).
- [31] G. Del Monte, A. Ninarello, F. Camerin, L. Rovigatti, N. Gnan, and E. Zaccarelli, *Soft Matter* **15**, 8113 (2019).
- [32] F. Brasili, G. Del Monte, A. Capocéfalo, E. Chauveau, E. Buratti, S. Casciardi, D. Truzzolillo, S. Sennato, and E. Zaccarelli, *ACS Applied Materials & Interfaces* **15**, 58770 (2023).
- [33] T. Soddemann, B. Dünweg, and K. Kremer, *The European Physical Journal E* **6**, 409 (2001).
- [34] P. K. Jain, W. Huang, and M. A. El-Sayed, *Nano letters* **7**, 2080 (2007).
- [35] C. Sönnichsen, B. M. Reinhard, J. Liphardt, and A. P. Alivisatos, *Nature biotechnology* **23**, 741 (2005).
- [36] D. Truzzolillo, S. Sennato, S. Sarti, S. Casciardi, C. Bazzoni, and F. Bordi, *Soft Matter* **14**, 4110 (2018).
- [37] D. Truzzolillo, V. Roger, C. Dupas, S. Mora, and L. Cipelletti, *Journal of Physics: Condensed Matter* **27**, 194103 (2015).
- [38] A. Guinier and G. Fournet, *Small-angle scattering of x-rays* (1955).
- [39] G. S. Grest and K. Kremer, *Physical Review A* **33**, 3628 (1986).

- [40] K. Kremer and G. S. Grest, *The Journal of Chemical Physics* **92**, 5057 (1990).
- [41] A. J. Moreno and F. L. Verso, *Soft Matter* **14**, 7083 (2018).
- [42] M. Deserno and C. Holm, *The Journal of Chemical Physics* **109**, 7678 (1998).
- [43] G. Del Monte, F. Camerin, A. Ninarello, N. Gnan, L. Rovigatti, and E. Zaccarelli, *Journal of Physics: Condensed Matter* **33**, 084001 (2020).
- [44] G. Del Monte, D. Truzzolillo, F. Camerin, A. Ninarello, E. Chauveau, L. Tavagnacco, N. Gnan, L. Rovigatti, S. Sennato, and E. Zaccarelli, *Proceedings of the National Academy of Sciences* **118**, e2109560118 (2021).
- [45] S. Plimpton, *Journal of computational physics* **117**, 1 (1995).
- [46] D. Juba, D. J. Audus, M. Mascagni, J. F. Douglas, and W. Keyrouz, *Journal of Research of National Institute of Standards and Technology* **122**, 10.6028/jres.122.020 (2017).